Research Article

ADVANCED PHOTONICS

Space-time refraction of space-time wave packets

Zeki Hayran* and John B. Pendry
Imperial College London, The Blackett Laboratory, Department of Physics, London, United Kingdom

Abstract. Refraction is usually understood as a boundary rule relating the direction and frequency of a wave across an interface. In space-time photonics, this picture is incomplete because both the medium and the wave can carry space-time structure. A space-time index modulation can form a synthetic moving boundary, whereas a space-time wave packet carries a prescribed group velocity through spatio-temporal spectral correlations. We show that their interaction is governed not by isolated spectral components alone, but by how the moving boundary transforms the geometry of the space-time spectrum as a whole. We develop a theory of space-time refraction for multiple space-time wave-packet families at a translating planar interface between homogeneous, nondispersive media. Even without material dispersion, and for the same two media and interface velocity, different packet families follow different group-velocity maps. This leads to effects with no spatial counterpart, including velocity compression, where many incident group velocities map to a narrow transmitted band, and velocity fission, where a single incident wave packet splits into two propagation-invariant branches with different velocities. The results identify moving interfaces as programmable transformations of structured light, with implications for programmable delay control, signal routing, controlled quantum emission, and analog-gravity platforms.

Keywords: space-time refraction; space-time wave packets; moving refractive index fronts; group velocity control; X–waves; space-time metamaterials; optical horizons; analog gravity.

Received Feb. 11, 2026; revised manuscript received May 14, 2026; accepted for publication Jun. 11, 2026; published online Jul. 9, 2026.

[DOI: 10.1117/1.AP.8.6.066001]

1 Introduction

Controlling the flow of electromagnetic waves is a central theme in optics and photonics. Traditionally, this control has relied on spatial structuring, from refractive components to photonic crystals and metasurfaces.[1–3] Time modulation provides a complementary route: in purely time-modulated media,[4] refractive index changes that are uniform in space but vary in time enable frequency conversion,[5,6] temporal reflection,[7,8] time-reversal,[9] and routes to overcome conventional limits.[10–14] Combining spatial and temporal variation extends this control further. Space-time modulation can produce quantum-emission processes,[15–17] nonreciprocal transport,[18] and analog Fresnel-drag effects,[19] as well as related phenomena.[20] Within this broader class, synthetic motion is especially relevant here: the modulation is designed so that the refractive-index profile drifts across space with a prescribed apparent velocity.[21–24] By programming the spatio-temporal modulation pattern, this synthetically moving boundary can be tuned from deeply subluminal to effectively superluminal,[21,22] providing a flexible and experimentally accessible way to realize effective moving interfaces in optical materials.

A complementary route is to engineer the electromagnetic wave rather than the medium. In this field-based approach, space-time wave packets (STWPs) provide the relevant structured fields: they are pulsed beams whose spatial and temporal frequencies are correlated so that the packet propagates without diffraction or dispersion.[25] In the light-cone construction used in the next section, these correlations are imposed by a tilted spectral plane, whose tilt fixes the axial group velocity.[25,26] Consequently, packets with the same carrier frequency and spatial profile can be launched with widely different group velocities.[27,28] This tunability creates a key degree of freedom for moving-boundary physics: the packet group velocity is set by the STWP spectral tilt, whereas the interface velocity is set independently by synthetic motion.[22] STWPs therefore provide a controlled platform for studying how structured light interacts with moving interfaces.

*Address all correspondence to Zeki Hayran, z.hayran@imperial.ac.uk

This two-velocity problem has seen only limited attention. A recent theoretical analysis showed that a moving refractive index front can strongly reshape a normally incident baseband STWP by changing its group velocity and spectral form.[29] Although this study highlighted the opportunities offered by moving boundaries for controlling structured fields, it focused on a single wave packet family. Other families, such as X–waves and sideband packets, are defined by different intersections with the light cone, respectively, through-origin and off-axis geometries.[25] These different geometries suggest qualitatively different refraction behaviour,[26] but their transformation across a moving interface and the influence of oblique incidence remain largely unexplored.

Here, we address this gap and develop a general theory of space-time refraction for baseband packets at arbitrary incidence and for X–wave and sideband packets at normal incidence. We identify the invariants that govern their transformation, obtain the corresponding refraction laws, and show how these laws connect continuously to both spatial- and temporal-interface limits, with derivations, validity conditions, and consistency checks presented in Sec. S1 in the Supplementary Material. The resulting framework clarifies the distinct behavior of different packet families, reveals singular conditions associated with optical horizons,[30–32] and provides a foundation for using STWPs to study dynamic media. To illustrate the range of possibilities, we present two example applications: "space-time optical push broom," in which a moving boundary compresses a wide spread of incident velocities into a narrow transmitted band, and "velocity spectral optical fission," in which an incident X–wave splits into two branches with distinct velocities.

2 Main

We begin by specifying the geometry of the moving interface and the STWPs to which the refraction laws apply. Figure 1(a) gives a three-dimensional (3D) view of an STWP interacting with a planar interface moving along z, whereas Fig. 1(b) shows the corresponding two-dimensional (2D) (x, z) section used to define the incidence angle ϕ_j and the spectral tilt angle θ_j. Figure 1(c) gives the associated (k_z, ω) construction, and Fig. 1(d) shows the space-time spectral geometry of the three STWP families in (k_x, k_z, ω) space. The analysis is formulated for light-sheet STWPs with one transverse coordinate x, whereas the field is uniform along y. This choice

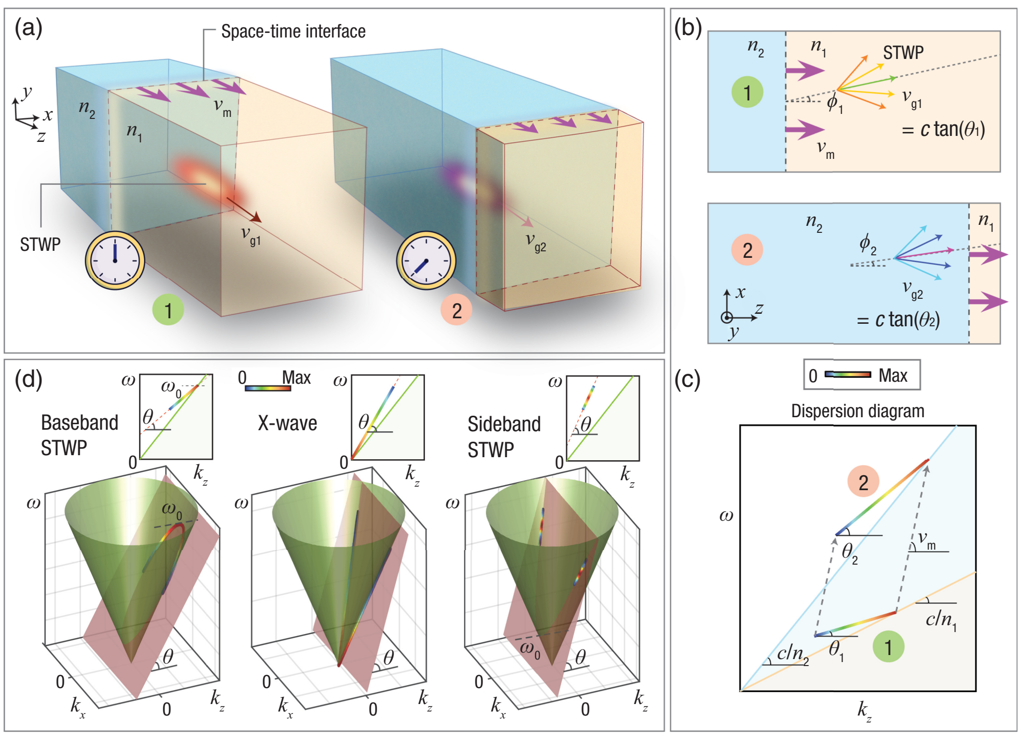

Fig. 1 Interaction of STWPs with a moving refractive index interface. (a) 3D schematic of an STWP crossing a planar space-time (ST) interface between media with refractive indices n_1 and n_2. The interface moves along z with velocity v_m, and the packet group velocity changes from v_{g1} to v_{g2}. (b) 2D (x, z) view defining the incidence angle ϕ_j and the spectral tilt angle θ_j, with $v_{gj} = c \tan \theta_j$. The former describes the real-space packet direction, whereas the latter fixes the STWP group velocity. (c) (k_z, ω) construction for baseband space-time refraction. The light lines of the two media have slopes c/n_1 and c/n_2, and the interface line has slope v_m; the conventional spatial-interface limit is recovered as $v_m \to 0$, when this line becomes horizontal. (d) Spectral geometries of the three STWP families. Top row: intersections in the (k_z, ω) section. Bottom row: 3D (k_x, k_z, ω) representation, with green cones denoting the light cones and colored curves defining the baseband, X-wave, and sideband families. In panels (c) and (d), the color scale denotes normalized spectral amplitude weight along the plotted curves.

fixes the transverse plane without loss of generality for the planar interface geometry considered here; a fully cylindrically symmetric STWP would require retaining both transverse wave-vector components.

The interface separates two homogeneous, nondispersive dielectrics with refractive indices n_1 and n_2. It is uniform along x and moves along z with velocity v_m, as sketched in Figs. 1(a) and 1(b). Medium 1 denotes the side occupied by the incident packet before it reaches the interface, and medium 2 denotes the side into which the transmitted packet emerges; these labels specify the incident and transmitted regions, not fixed positions along z. The packet axes form angles ϕ_1 and ϕ_2 with the interface normal, with $\phi_1 = \phi_2 = 0$ corresponding to normal incidence. Throughout we assume an impedance-matched interface, either through matched ε and μ or through an adiabatic transition, so that reflection is negligible. Without this assumption, the same kinematic laws apply, but reflected channels and amplitude reshaping must also be included.

The refraction process is governed by two interface invariants. Uniformity along x conserves k_x. In addition, the boundary depends on the co-moving coordinate $s = z - v_m t$. For a plane-wave factor $e^{i(k_z z-\omega t)}$, substituting $z = s + v_m t$ gives $e^{i[k_z s+(k_z v_m-\omega)t]}$. Phase matching on the moving boundary therefore conserves $k_z v_m - \omega$, or equivalently,

$$T = k_z - \frac{\omega}{v_m}, \tag{1}$$

where k_z is the normal wave-vector component and ω is the angular frequency. Space-time refraction is then obtained by imposing equality of k_x and T on the two sides, together with the dispersion relations. In the limit $v_m \to 0$, this reduces to conservation of k_x and ω; in the limit $v_m \to \infty$, it becomes conservation of k_x and k_z, as for a purely temporal index jump. Figure 1(c) gives the corresponding graphical construction: the medium light line is combined with the interface line set by v_m, whereas the spectral-plane constraint of the STWP supplies the remaining condition needed to obtain the refraction law.

The STWPs considered here are propagation-invariant pulsed beams obtained by intersecting the light cone of a uniform nondispersive medium with tilted spectral planes. The light cone is $k_x^2 + k_z^2 = (n\omega/c)^2$, and the plane tilt in the $(k_z, \omega/c)$ projection fixes the group index,

$$\tilde{n} = \frac{c}{v_g} = \cot\theta, \tag{2}$$

where v_g is the axial group velocity and θ is the spectral tilt. This spectral tilt should be distinguished from the incidence angle: θ_j fixes the orientation of the STWP spectrum in the (k_z, ω) plane and hence the group velocity, whereas ϕ_j gives the real-space direction of the packet axis relative to the interface normal. This nondispersive light-cone construction is the model used in the present moving-interface theory; it should not be read as a general limitation of STWPs, whose propagation and refraction have also been extended to dispersive media.[33,34] The three families, shown schematically in Fig. 1(d), correspond to different intersections between a tilted spectral plane and the light cone: baseband packets are associated with a near-axis intersection around a carrier point [Fig. 1(d), left], X–waves with a through-origin intersection [Fig. 1(d), middle], and sideband packets with an off-axis intersection at finite transverse wave number and frequency offset [Fig. 1(d), right]. These three cases are defined more precisely in the following paragraphs.

Baseband STWPs are the closest STWP analog of conventional pulsed beams. Their spectral plane intersects the light cone near an on-axis carrier, so the spectral locus passes through $k_x \approx 0$ and $\omega \approx \omega_0$ [Fig. 1(d), left].[26,27] Changing the spectral tilt then tunes the group velocity from subluminal to luminal or superluminal values.

X–wave STWPs form a second family [Fig. 1(d), middle]. Their spectral plane passes through the origin, producing straight-line branches in the $(k_x, \omega/c)$ projection.[26] The branches at $\pm k_x$ give an X-shaped propagation-invariant profile.[35–37] Their group velocity is superluminal relative to the host medium, meaning faster than c/n, not necessarily faster than c. This through-origin geometry makes X–waves an exact nonparaxial STWP family, although they are more challenging to synthesize than baseband packets.[26]

Sideband STWPs constitute a third family [Fig. 1(d), right]. Their spectral plane intersects the light cone away from both the origin and the $k_x = 0$ axis, so the spectrum occupies an off-axis conic segment at finite transverse wave number and finite frequency offset.[26,38] These packets are described by an effective group index $\tilde{n}$ and a sideband parameter ζ, which measures the frequency-axis offset between the carrier point and the origin.[26] Sideband packets therefore provide an off-axis STWP family that approaches the X–wave limit when the spectral plane approaches the through-origin geometry.

Previous work derived time-invariant refraction laws at normal incidence for all three STWP families, whereas oblique incidence was treated in detail only for baseband packets.[26] Here, the oblique baseband treatment is likewise restricted to the narrowband, paraxial regime, where Δk_x remains small. Broader baseband spectra can distort under oblique incidence. For X–wave and sideband packets, oblique incidence breaks the symmetry of their off-axis lobes, and moving-interface phase matching adds further skewing. We therefore treat oblique incidence only for baseband STWPs, whereas X–wave and sideband STWPs are treated at normal incidence. With this scope fixed, we now formulate the corresponding space-time refraction laws and examine how they interpolate between spatial and purely temporal limits.

2.1 Baseband Space-Time Refraction Law

We first consider baseband STWPs in the narrowband, paraxial regime around the on-axis carrier [Fig. 1(d), left]. We denote by n_1 and n_2 the refractive indices of the incident and transmitted media, respectively, by $\tilde{n}_1$ and $\tilde{n}_2$ the corresponding group indices, and by ϕ_1 and ϕ_2 the corresponding incidence and refraction angles. We also define the dimensionless interface parameter $\xi = c/v_m$.

Applying conservation of k_x and $T = k_z - \omega/v_m$, expanding the baseband spectrum about the on-axis carrier, and matching the even quadratic term in the paraxial mapping gives the oblique baseband refraction law,

$$\frac{(\xi - \tilde{n}_1 \cos\phi_1)(n_1 \cos\phi_1 - \xi)}{n_1(\tilde{n}_1 - n_1)\cos^2\phi_1} = \frac{(\xi - \tilde{n}_2 \cos\phi_2)(n_2 \cos\phi_2 - \xi)}{n_2(\tilde{n}_2 - n_2)\cos^2\phi_2}, \tag{3}$$

which, together with the carrier phase-matching constraints, gives an implicit map from $(\tilde{n}_1, \phi_1)$ to $(\tilde{n}_2, \phi_2)$. At normal incidence, $\phi_1 = \phi_2 = 0$, Eq. (3) reduces to

$$\frac{(\xi - \tilde{n}_1)(n_1 - \xi)}{n_1(\tilde{n}_1 - n_1)} = \frac{(\xi - \tilde{n}_2)(n_2 - \xi)}{n_2(\tilde{n}_2 - n_2)}, \tag{4}$$

which directly relates the incident and transmitted group indices, in agreement with Ref. 29. The derivation of Eq. (3), including the carrier constraints, paraxial expansion, oblique-incidence distortion terms, and spatial- and temporal-interface limits, is given in Sec. S1 in the Supplementary Material.

Beyond giving the transmitted group index, Eq. (3) also reveals the structure of the baseband velocity map. The factor $\xi - \tilde{n}_j \cos \phi_j$ controls the even curvature of the Doppler invariant across the paraxial spectrum. Its zero, $\tilde{n}_j \cos \phi_j = \xi$, marks a curvature-zero point where the local mapping changes character. At normal incidence this reduces to the co-moving condition $\tilde{n}_j = \xi$. This exact co-moving point is best understood as a limiting phase-matched fixed point, because a packet with zero relative velocity to a sharp interface does not undergo an ordinary crossing event unless it initially overlaps the transition region. More importantly for the applications below, the same map can become nearly flat away from this fixed point: for suitable choices of ξ, including values between n_1 and n_2, Eq. (4) compresses a broad range of incident group indices into a narrow transmitted range. This velocity-compression regime underlies the "space-time optical push broom" effect discussed in Sec. 3; further details on the mapping slope, accumulation behavior, and co-moving fixed points are given in Sec. S2 in the Supplementary Material.

2.2 X–wave Space-Time Refraction Law

X–wave STWPs are described by a through-origin spectral plane whose intersection with the light cone gives straight-line branches symmetric in k_x [Fig. 1(d), middle]. As a result, the relations between (k_x, k_z, ω) and the group index $\tilde{n}$ are linear along each branch, and the moving-interface refraction law can be obtained without a paraxial expansion.[25,26] For a moving interface that is uniform along x and travels along z with velocity v_m, conservation of k_x and $k_z - \omega/v_m$, together with the dispersion relations, gives

$$\frac{\tilde{n}_1 - \xi}{\sqrt{n_1^2 - \tilde{n}_1^2}} = \frac{\tilde{n}_2 - \xi}{\sqrt{n_2^2 - \tilde{n}_2^2}}, \tag{5}$$

with existence domain $n_j^2 - \tilde{n}_j^2 > 0$ and $\xi = c/v_m$. The derivation of Eq. (5), its spatial and temporal limits, its co-moving resonance, and the restriction to normal incidence are given in Sec. S1 in the Supplementary Material. The numerator vanishes at $\tilde{n}_j = \xi$, which is the X–wave co-moving phase-matched condition. As for baseband STWPs at normal incidence, this is a limiting fixed point rather than an ordinary refraction event, because a packet exactly co-moving with the interface does not cross it unless it initially overlaps the transition region.

The main consequence of Eq. (5) is that the transmitted group index $\tilde{n}_2$ satisfies a quadratic equation. For suitable $(n_1, n_2, \tilde{n}_1, \xi)$, two physical roots can lie inside the X–wave existence domain, so one incident X–wave can generate two transmitted X–wave branches with different spectral tilts and group velocities. This velocity fission is analyzed in Sec. 3, with the quadratic form, discriminant, physical-domain conditions, and real-space manifestation given in Sec. S3 in the Supplementary Material. This branch structure is kinematic: Eq. (5) determines the allowed transmitted X–wave supports, but not the amount of field coupled into each one. The branch amplitudes depend on the boundary conditions and on the implementation of the interface, and a sharp-interface amplitude-partition model is given in Sec. S3.4 in the Supplementary Material. Finally, Eq. (5) should not be viewed as a regular limit of the baseband law: the baseband result follows from a narrowband paraxial expansion near $k_x = 0$, whereas the X–wave law follows from the exact through-origin nonparaxial support.

2.3 Sideband Space-Time Refraction Law

Sideband STWPs form an off-axis family: their spectral plane intersects the light cone away from both the origin and the $k_x = 0$ axis, giving a conic segment at finite transverse wave number and finite frequency offset [Fig. 1(d), right]. We describe them by an effective group index $\tilde{n}$ and a sideband parameter ζ, with $\zeta = 1 - \omega_0/\omega_c$, where ω_c is the carrier frequency of the sideband segment. Because the spectral plane does not pass through the origin, matching the carrier point and matching the local spectral slope are separate requirements.

In the narrowband regime, the slope-matching condition at normal incidence is

$$\begin{aligned}(1 - \zeta_2)(n_1 + \tilde{n}_1)(n_1 - \zeta_1\tilde{n}_1)(\tilde{n}_2 - \xi) \\ = (1 - \zeta_1)(n_2 + \tilde{n}_2)(n_2 - \zeta_2\tilde{n}_2)(\tilde{n}_1 - \xi),\end{aligned} \tag{6}$$

where ζ_1 and ζ_2 label the incident and transmitted sideband packets, $1 - \zeta_j > 0$, the carrier transverse wave number $k_{cx,j}$ is real, and $\xi = c/v_m$. Equation (6) is a local slope condition obtained after linearizing the sideband conic about its carrier. A physical transmitted sideband STWP must also satisfy the carrier phase-matching constraints: conservation of the tangential carrier component k_{cx} for the chosen lobe, and conservation of the Doppler carrier invariant $k_{cz} - \xi k_c$. These carrier constraints fix how the center of the sideband conic is mapped, whereas Eq. (6) fixes how its local slope is mapped. Because the transmitted sideband ansatz has only two free parameters, $(\tilde{n}_2, \zeta_2)$, the two carrier constraints and the slope condition form an overconstrained set for finite $1 - \zeta_j$. They are therefore not generically compatible, except in special tuned cases or in the X–wave limit, in which the carrier and slope constraints collapse onto the same through-origin geometry.

Thus, solving Eq. (6) alone gives only candidate slope fits. At fixed ζ_2, it is quadratic in $\tilde{n}_2$, so two algebraic roots may appear, but they correspond to physical transmitted sideband packets only if the carrier constraints and sideband existence conditions are also satisfied. In the limit $\zeta_j \to 1$, the sideband plane approaches the through-origin X–wave geometry, the carrier and slope constraints merge, and Eq. (6) reduces to the X–wave law in Eq. (5). Sideband packets therefore provide an off-axis route to the X–wave limit, rather than a continuation of the baseband law. The derivation of Eq. (6), the carrier constraints, the spatial, temporal, and X–wave limits, the quadratic roots, and the sideband existence conditions are given in Sec. S1 in the Supplementary Material.

3 Applications

3.1 Space-Time Optical Push Broom

The baseband refraction law can compress velocity content when the normal-incidence map in Eq. (4) has a small slope over a finite range of input group indices. In this regime, incident baseband STWPs with different group velocities are refracted into transmitted packets with nearly the same group velocity. We refer to this velocity-compression regime as a space-time optical push broom.

Earlier optical push-broom schemes use moving refractive-index fronts in dispersive guided structures to compress pulses, translate frequencies, or produce large effective delays, with applications in optical buffering, pulse shaping, and all-optical switching.[21,39–44] In those schemes, the front velocity is usually tied to the pump propagation, whereas the signal velocity is fixed by material or waveguide dispersion. The relative speed between the front and the probe is therefore only weakly tunable. Here, baseband STWPs set the packet group index through the spectral tilt, whereas synthetic motion sets the apparent interface velocity v_m independently.[22] Reference 22 demonstrates programmable synthetic motion in a surface-localized geometry rather than the rigidly translating bulk interface considered here; a closer implementation would use a guided or thin-film platform with in-plane STWP propagation and in-plane synthetic motion, with out-of-plane confinement.[45] This separation of packet velocity and interface velocity enables velocity compression in a propagation-invariant setting, without relying on the material-dispersion constraints of conventional push-broom schemes. A quantitative analysis of the mapping slope, accumulation of incident group indices, and design conditions is given in Sec. S2 in the Supplementary Material.

The push-broom regime is selected by targeting flat portions of the normal-incidence map in Eq. (4), where a finite interval of incident group indices is mapped to a narrow transmitted interval. This occurs when the interface parameter ξ places the transmitted group indices near an accumulation region of the map while avoiding exact luminal or co-moving singular points; the quantitative slope and design conditions are given in Sec. S2 in the Supplementary Material. Figure 2 shows one such example for normally incident baseband STWPs crossing a moving interface with $n_1 = 1$, $n_2 = 2$, and $v_m = 0.6c$, so that $\xi \simeq 1.67$. For these parameters, Eq. (4) gives a nearly flat $\theta_2(\theta_1)$ curve over a wide range of incident tilts [Fig. 2(a)], so a broad set of incident group indices in medium 1 maps to a narrow transmitted range in medium 2. Both the small-angle and large-angle plateaus in Fig. 2(a) are compression branches. We focus on the small-angle branch, where the transmitted packets remain slower than the interface; the large-angle branch gives a complementary pull-through regime in which the transmitted packets are faster than the interface. The steep intervening region is expansive, so small changes in incident tilt produce large changes in transmitted group velocity. The two representative inputs marked in Fig. 2(a), STWP-1 and STWP-2, lie on the small-angle compression branch and have clearly different incident group velocities.

The same mapping is visible in the spectral construction of Fig. 2(b). The light cones of the two media and the space-time refraction plane determine the transmitted spectral sheet associated with each incident sheet. For the chosen parameters, carrier phase matching gives

$$\frac{\omega_2}{\omega_1} = \frac{n_1 - \xi}{n_2 - \xi}, \tag{7}$$

which is negative because $n_1 < \xi < n_2$. The mapped spectrum therefore lies on the negative-frequency branch of the n_2 cone. In the specific realization of Fig. 2, velocity compression is therefore accompanied by transverse phase conjugation: the signed component $(k_x, -k_z, -\omega)$ is equivalently represented at positive frequency as $(-k_x, k_z, \omega)$. Thus, the compression follows from Eq. (4), whereas this parameter choice realizes it through reversal of the transverse wave-vector component. The algebra and the negative-frequency interpretation are given in Sec. S2.4 in the Supplementary Material.

The real-space trajectories in Fig. 2(c) show both the velocity compression and the anomalous nature of the mapping. We call this regime anomalous because the transmitted packets enter the higher-index medium but do not slow down in the usual sense. In a uniform medium, STWP-1 and STWP-2 separate because their group velocities are different. After crossing the moving interface, they instead follow nearby transmitted world lines, consistent with the nearly constant transmitted group index predicted by Eq. (4). Thus, despite $n_2 > n_1$, the transmitted group velocities increase and become nearly matched. Field snapshots in Fig. 2(d) confirm that the two packets remain close after transmission and propagate with nearly matched velocities in medium 2 (see Video 1).

Together, the spectral and real-space pictures show that a single moving interface can compress a broad set of input STWP velocities into a narrow transmitted band. By tuning v_m, n_1, and n_2, the compression can be obtained without operating arbitrarily close to the luminal limit, whereas suitable parameter choices can also access negative-frequency and phase-conjugated branches. More generally, this ability to remap the velocity content of structured pulses suggests routes to compact time gating, programmable delay control, and signal routing in space-time photonic platforms.

3.2 Velocity Spectral Optical Fission

The X–wave refraction law at normal incidence, Eq. (5), can be double valued in the transmitted group index. For suitable $(n_1, n_2, v_m, \tilde{n}_1)$, the quadratic equation for $\tilde{n}_2$ has two physical roots inside the X–wave existence domain. A single incident X–wave can then generate two propagation-invariant transmitted X–waves with different spectral tilts and group velocities. We call this process "velocity spectral optical fission." The quadratic form, discriminant analysis, and physical-domain conditions are summarized in Sec. S3 in the Supplementary Material.

Figure 3 shows this effect for $n_1 = 1.5$, $n_2 = 1.0$, and $v_m = 0.5c$. The refraction curve $\theta_2(\theta_1)$ is single valued over most of the incident range, but becomes double valued in the green band of Fig. 3(a). In this interval, both transmitted solutions satisfy the X–wave existence condition. The two output branches, labeled STWP-1 and STWP-2, therefore have different spectral tilt angles and different group velocities in medium 2.

The spectral construction in Fig. 3(b) shows the origin of the splitting. For a fixed conserved k_x, the Doppler invariant and the medium-2 dispersion relation can admit two allowed (k_z, ω) solutions; the white marker and arrows show one such mapping. Applying this pointwise mapping across the incident X–wave

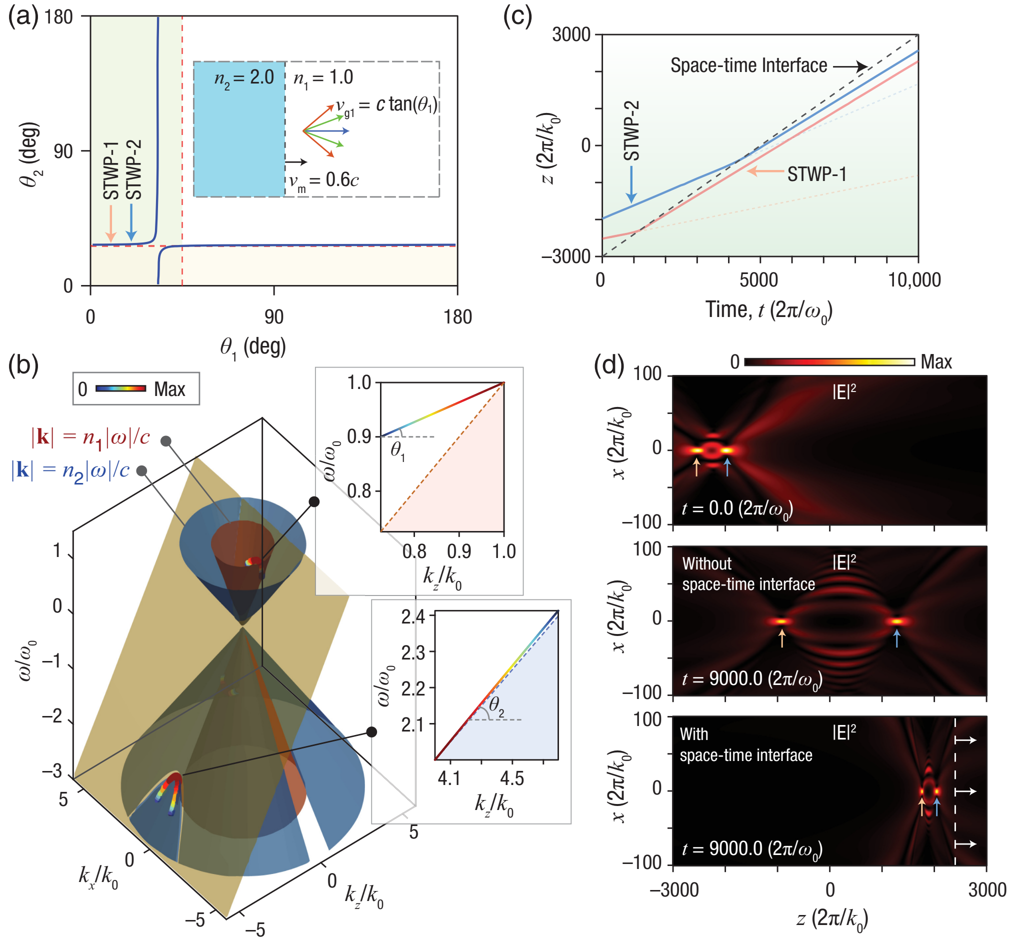

Fig. 2 Space-time optical push broom in an anomalous refraction regime. (a) Baseband space-time refraction law at normal incidence for $n_1 = 1$, $n_2 = 2$, and $v_m = 0.6c$. The map $\theta_1 \rightarrow \theta_2$ compresses a broad range of incident group indices into a narrow transmitted range. Green and yellow shadings denote the subluminal sectors in media 1 and 2, and red dashed lines denote the luminal conditions. Orange and blue arrows mark representative inputs. Inset, incidence geometry. (b) Spectral construction in (k_x, k_z, ω) space. Red and blue cones denote the light cones of media 1 and 2, and the yellow plane is the space-time refraction plane. Insets show the corresponding (k_z, ω) projections. The color scale denotes normalized spectral amplitude weight along the plotted spectra. (c) World lines of the interface and packet centers at $x = 0$. Dashed black, interface trajectory. Solid orange and blue, trajectories with the interface. Dotted lines, reference propagation without the interface. (d) Field intensity snapshots $|E|^2$ in the (x, z) plane, showing input, separation in a uniform medium, and near copropagation after transmission. The dashed vertical line marks the interface, and arrows track the packet peaks (see Video 1, GIF, 5.39 MB [URI: https://doi.org/10.1117/1.AP.8.6.066001.s1]).

spectrum gives two transmitted spectral branches, each with a different (k_z, ω) slope and therefore a different group velocity. The world lines in Fig. 3(c) show the corresponding separation in real space: both transmitted branches move faster than the interface for the parameters used here, but at different speeds. Field snapshots in Fig. 3(d) show two separated X-shaped intensity profiles after transmission, consistent with the predicted group velocities (see Video 2). The slight waviness in $|E|^2$ arises from coherent beating between the two transmitted branches and finite-window sidelobes; each branch separately remains supported on a one-dimensional X–wave spectral support. This splitting is specific to a moving interface: a static interface conserves ω and k_x, giving a unique forward transmitted component, whereas the moving-interface invariant $k_z - \omega/v_m$ can allow two forward transmitted solutions. More generally, velocity fission shows that a moving interface can convert one incident propagation-invariant channel into multiple transmitted velocity channels. This capability suggests compact velocity multiplexing, programmable delay, and multichannel signal-processing operations based on space-time structured waves.

4 Discussion and Outlook

Space-time refraction is usually formulated in terms of how individual spectral components transform at a moving boundary.[46] For structured pulses, this component-wise picture

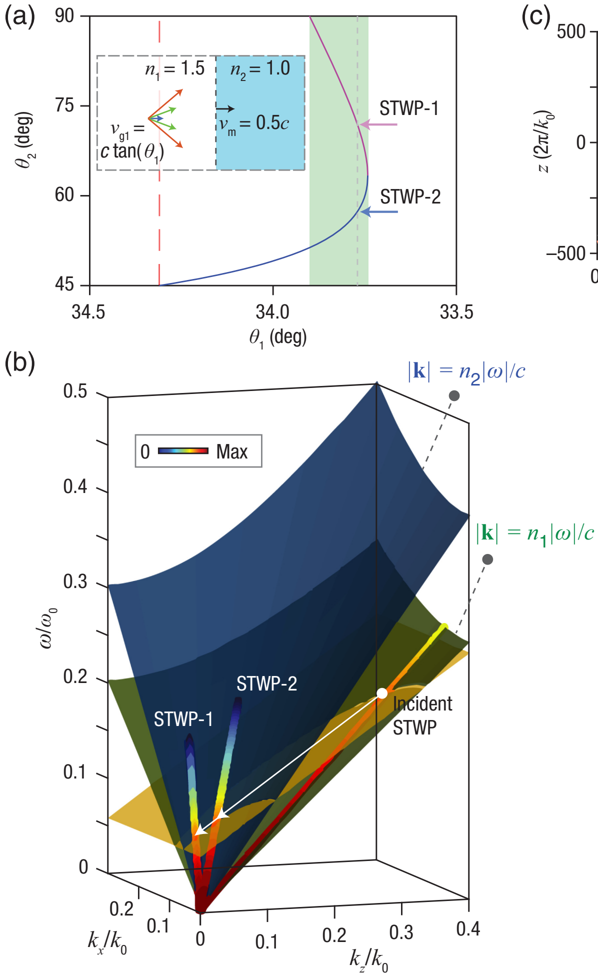

Fig. 3 Velocity spectral optical fission of an X–wave at a moving space-time interface. (a) Normal-incidence X–wave refraction law for $n_1 = 1.5$, $n_2 = 1.0$, and $v_m = 0.5c$. The map $\theta_1 \to \theta_2$ becomes double valued in the green band, so one incident X–wave produces two transmitted branches. Magenta and blue arrows mark representative outputs from a single input. Inset, incidence geometry. (b) Spectral construction in (k_x, k_z, ω) space. Green and blue cones denote the light cones of media 1 and 2, and the yellow plane denotes the Doppler phase-matching constraint. The white arrow marks the pointwise mapping of one incident spectral component; at fixed conserved k_x and Doppler invariant T, the medium-2 cone admits two allowed (k_z, ω) solutions, generating two transmitted X–wave branches. The color scale denotes normalized spectral amplitude weight along the plotted spectra. Only the physical octant $k_x, k_z, \omega > 0$ is shown. (c) World lines at $x = 0$. Dashed black, interface trajectory. Orange, incident X–wave. Magenta and blue, transmitted branches separating according to their different group velocities. (d) Field intensity snapshots $|E|^2$ at $t = 0$, $240(2\pi/\omega_0)$, and $414(2\pi/\omega_0)$. The dashed line marks the interface, and arrows track STWP-1 and STWP-2 (see Video 2, GIF, 1.05 MB [URI: https://doi.org/10.1117/1.AP.8.6.066001.s2]).

is incomplete: the conserved quantities transform the geometry of the space-time spectrum as a whole. The STWP families considered here show that this spectral geometry can produce different group-velocity mappings even under the same boundary invariants. Moving interfaces can therefore reorganize the velocity content of structured fields through the interplay between boundary motion and space-time spectral correlations, rather than through the interface velocity alone.

The conserved-quantity picture developed here uses the simplest setting: light-sheet STWPs in homogeneous nondispersive media. This choice makes the spectral construction analytically explicit, because the wave packet spectrum lies on a simple light cone and the moving interface imposes linear phase-matching constraints. It also identifies the main routes for future extension. One route is to include material and platform complexity, especially dispersive media, where related stationary-interface results already exist,[33,34] and guided or inhomogeneous platforms that are closer to experiments.[45] More generally, broad transverse or temporal bandwidths, especially at oblique incidence, may require going beyond the leading paraxial and narrowband description to account for skewing, waveform distortion, and effective group-velocity dispersion. A second route is to extend the conserved-quantity approach to other structured waves. The present formulation does not directly cover generic Airy beams,[47] Airy–Bessel bullets,[48] or spatiotemporal vortices with transverse orbital angular momentum[49,50]; nevertheless, Bessel-type packets and vortex-carrying STWPs are natural candidates for future work because similar invariants could be used to track how a moving interface changes their cone angle, transverse wave number, or topological charge content.

Experimental implementations should aim to produce a measurable change in the STWP spectral tilt or group velocity, rather than an order-unity or perfectly abrupt index step. In the kinematic description used here, the mapping is set primarily by the initial and final refractive indices and by the interface velocity, whereas finite transition sharpness mainly affects secondary scattering and waveform fidelity. Kerr/XPM-induced moving perturbations can provide proof-of-principle realizations.[51] Optically driven TCO fronts[22] and synchronized electro-optic modulation[52] provide complementary routes to larger ultrafast index changes or more programmable synthetic motion. In such platforms, STWPs provide a controlled way to tune the incident group velocity relative to the boundary, enabling tests of horizon-like conditions,[31] dynamical energy flow in time-varying quantum electrodynamics,[32] and quantum emission from superluminal[15] or accelerating index perturbations.[16]

5 Appendix: Methods

5.1 Numerical Simulations

Numerical results were obtained from a spectral moving-interface reconstruction. Each field was written as a finite discrete sum of plane waves sampled from the analytic STWP spectral support. At the translating interface, each spectral component was mapped by conserving k_x and $T = k_z - \omega/v_m$, and the transmitted component was then selected from the dispersion relation in medium 2. The input spectral weights were real and even in k_x, with no imposed spectral phase apart from propagation phase and a constant offset used to maintain phase continuity at the initial interface position. The finite spectral windows, apodization functions, bandwidth definitions, and all figure-specific numerical parameters are given in Sec. S4 in the Supplementary Material.

5.2 Supplementary Information

Section S1 in the Supplementary Material gives the derivations and limiting cases of the refraction laws, Sec. S2 in the Supplementary Material analyzes the space-time optical push broom, Sec. S3 in the Supplementary Material details X–wave fission and amplitude partition, and Sec. S4 in the Supplementary Material summarizes the numerical spectral windows and reconstruction parameters.

Disclosures

The authors declare no competing interests.

Code and Data Availability

The code used to produce these results is available from the corresponding author upon reasonable request. Authors confirm that all relevant data are included in the paper and/or its Supplementary Material files.

Acknowledgments

Z. H. and J. B. P. acknowledge support from the Engineering and Physical Sciences Research Council (EPSRC) under Grant No. EP/Y015673/1.

References

1. N. I. Zheludev and Y. S. Kivshar, “From metamaterials to metadevices,” *Nat. Mater.* **11**(11), 917–924 (2012).
2. C. Simovski and S. Tretyakov, *An Introduction to Metamaterials and Nanophotonics*, Cambridge University Press, Cambridge, UK (2020).
3. M. Butt, S. N. Khonina, and N. Kazanskiy, “Recent advances in photonic crystal optical devices: a review,” *Opt. Laser Technol.* **142**, 107265 (2021).
4. E. Galiffi et al., “Photonics of time-varying media,” *Adv. Photonics* **4**(1), 014002 (2022).
5. Z. Hayran, A. Chen, and F. Monticone, “Spectral causality and the scattering of waves,” *Optica* **8**(8), 1040–1049 (2021).
6. R. Tirole et al., “Second harmonic generation at a time-varying interface,” *Nat. Commun.* **15**(1), 7752 (2024).
7. H. Moussa et al., “Observation of temporal reflection and broadband frequency translation at photonic time interfaces,” *Nat. Phys.* **19**(6), 863–868 (2023).
8. T. R. Jones et al., “Time-reflection of microwaves by a fast optically-controlled time-boundary,” *Nat. Commun.* **15**(1), 6786 (2024).
9. S. Vezzoli et al., “Optical time reversal from time-dependent epsilon-near-zero media,” *Phys. Rev. Lett.* **120**(4), 043902 (2018).
10. Z. Hayran and F. Monticone, “Using time-varying systems to challenge fundamental limitations in electromagnetics: overview and summary of applications,” *IEEE Antennas Propag. Mag.* **65**(4), 29–38 (2023).
11. A. Shlivinski and Y. Hadad, “Beyond the bode-fano bound: wideband impedance matching for short pulses using temporal switching of transmission-line parameters,” *Phys. Rev. Lett.* **121**(20), 204301 (2018).
12. C. Firestein, A. Shlivinski, and Y. Hadad, “Absorption and scattering by a temporally switched lossy layer: going beyond the Rozanov bound,” *Phys. Rev. Appl.* **17**(1), 014017 (2022).
13. Z. Hayran and F. Monticone, “Beyond the Rozanov bound on electromagnetic absorption via periodic temporal modulations,” *Phys. Rev. Appl.* **21**(4), 044007 (2024).
14. M. Ciabattoni, Z. Hayran, and F. Monticone, “Observation of broadband super-absorption of electromagnetic waves through space-time symmetry breaking,” *Sci. Adv.* **11**(3), 7407 (2025).
15. F. Belgiorno et al., “Quantum radiation from superluminal refractive-index perturbations,” *Phys. Rev. Lett.* **104**(14), 140403 (2010).
16. J. Sloan et al., “Controlling two-photon emission from superluminal and accelerating index perturbations,” *Nat. Phys.* **18**(1), 67–74 (2022).
17. J. Pendry and S. A. Horsley, “QED in space–time varying materials,” *APL Quantum* **1**(2), 020901 (2024).
18. Z. Yu and S. Fan, “Complete optical isolation created by indirect interband photonic transitions,” *Nat. Photonics* **3**(2), 91–94 (2009).
19. P. A. Huidobro et al., “Fresnel drag in space–time-modulated metamaterials,” *Proc. Natl. Acad. Sci.* **116**(50), 24943–24948 (2019).
20. N. Engheta, “Four-dimensional optics using time-varying metamaterials,” *Science* **379**(6638), 1190–1191 (2023).
21. M. A. Gaafar et al., “Front-induced transitions,” *Nat. Photonics* **13**(11), 737–748 (2019).
22. A. Harwood et al., “Space-time optical diffraction from synthetic motion,” *Nat. Commun.* **16**(1), 5147 (2025).
23. Z. Hayran et al., “Pulse-driven photonic transitions and nonreciprocity in space-time modulated metasurfaces,” *ACS Photonics* **13**(5), 1343–1353 (2026).

24. Y. Vaddi et al., "Parametric amplification of optical pulses through synthetic motion in a time-varying medium," *Nano Lett.*, in press (2026).
25. M. Yessenov et al., "Space-time wave packets," *Adv. Opt. Photonics* **14**(3), 455–570 (2022).
26. M. Yessenov, B. Bhaduri, and A. F. Abouraddy, "Refraction of space-time wave packets: I. Theoretical principles," *J. Opt. Soc. Am. A* **38**(10), 1409–1422 (2021).
27. S. Longhi, "Gaussian pulsed beams with arbitrary speed," *Opt. Express* **12**(5), 935–940 (2004).
28. A. Sainte-Marie, O. Gobert, and F. Quere, "Controlling the velocity of ultrashort light pulses in vacuum through spatio-temporal couplings," *Optica* **4**(10), 1298–1304 (2017).
29. H. Wang, C. Guo, and S. Fan, "Spatiotemporal steering of nondiffracting wave packets," *Phys. Rev. Lett.* **134**(7), 073803 (2025).
30. T. G. Philbin et al., "Fiber-optical analog of the event horizon," *Science* **319**(5868), 1367–1370 (2008).
31. J. Drori et al., "Observation of stimulated hawking radiation in an optical analogue," *Phys. Rev. Lett.* **122**(1), 010404 (2019).
32. S. A. Horsley and J. B. Pendry, "Quantum electrodynamics of time-varying gratings," *Proc. Natl. Acad. Sci.* **120**(36), 2302652120 (2023).
33. M. Yessenov et al., "Refraction of space–time wave packets in a dispersive medium," *Opt. Lett.* **47**(7), 1630–1633 (2022).
34. H. He, C. Guo, and M. Xiao, "Nondispersive space–time wave packets propagating in dispersive media," *Laser Photonics Rev.* **16**(10), 2100634 (2022).
35. P. Saari and K. Reivelt, "Evidence of X-shaped propagation-invariant localized light waves," *Phys. Rev. Lett.* **79**(21), 4135–4138 (1997).
36. J.-Y. Lu and J. F. Greenleaf, "Nondiffracting X waves-exact solutions to free-space scalar wave equation and their finite aperture realizations," *IEEE Trans. Ultrason. Ferroelectr. Freq. Control* **39**(1), 19–31 (1992).
37. M. A. Porras and P. Di Trapani, "Localized and stationary light wave modes in dispersive media," *Phys. Rev. E Stat. Nonlinear Soft Matter Phys.* **69**(6), 066606 (2004).
38. J. N. Brittingham, "Focus waves modes in homogeneous Maxwell's equations: transverse electric mode," *J. Appl. Phys.* **54**(3), 1179–1189 (1983).
39. C. M. Sterke, "Optical push broom," *Opt. Lett.* **17**(13), 914–916 (1992).
40. N. Broderick et al., "Optical pulse compression in fiber Bragg gratings," *Phys. Rev. Lett.* **79**(23), 4566–4569 (1997).
41. K. Kondo and T. Baba, "Dynamic wavelength conversion in copropagating slow-light pulses," *Phys. Rev. Lett.* **112**(22), 223904 (2014).
42. A. W. Schiff-Kearn et al., "Front-induced transitions control THz waves," *Commun. Phys.* **4**(1), 162 (2021).
43. J. Pendry, "Air conditioning for photons," *Opt. Mater. Express* **14**(2), 407–413 (2024).
44. B. Zhang et al., "Pulse compression by a refractive index front in periodically modulated silicon waveguide," *Phys. Rev. A* **113**(1), 013515 (2026).
45. A. Shiri et al., "Hybrid guided space-time optical modes in unpatterned films," *Nat. Commun.* **11**(1), 6273 (2020).
46. C. Caloz and Z.-L. Deck-Léger, "Spacetime metamaterials—part I: general concepts," *IEEE Trans. Antennas Propag.* **68**(3), 1569–1582 (2019).
47. N. K. Efremidis et al., "Airy beams and accelerating waves: an overview of recent advances," *Optica* **6**(5), 686–701 (2019).
48. A. Chong et al., "Airy–Bessel wave packets as versatile linear light bullets," *Nat. Photonics* **4**(2), 103–106 (2010).
49. A. Chong et al., "Generation of spatiotemporal optical vortices with controllable transverse orbital angular momentum," *Nat. Photonics* **14**(6), 350–354 (2020).
50. W. Chen et al., "Time diffraction-free transverse orbital angular momentum beams," *Nat. Commun.* **13**(1), 4021 (2022).
51. R. Yanagimoto et al., "Temporal trapping: a route to strong coupling and deterministic optical quantum computation," *Optica* **9**(11), 1289–1296 (2022).
52. M. Yu et al., "Integrated femtosecond pulse generator on thin-film lithium niobate," *Nature* **612**(7939), 252–258 (2022).

Zeki Hayran received his PhD from Cornell University, where he was a Fulbright Scholar. He is currently a research associate at Imperial College London, where he conducts theoretical research on classical and quantum light control in nanophotonic structures. His past and present work spans time-varying metamaterials, non-Hermitian optics, topological photonics, and optical computing.

John B. Pendry is a condensed matter theorist. He is generally regarded as the founder of the field of metamaterials, materials that owe their properties to internal structure rather than chemical composition. They enable remarkable properties such as negative refractive index, lenses that break the diffraction limit, and a prototype cloaking device, which have caught the imagination of the world's media. His most recent work adds the dimension of time to their structure: META4D.